

Isothermal High-Temperature Oxidation Behaviour of Nickel-Based Superalloy IN740H

R. K. Singh¹  · S. Paswan²

Received: 2 April 2023 / Accepted: 7 December 2023 / Published online: 20 January 2024
© The Indian Institute of Metals - IIM 2024

Abstract The isothermal oxidation behaviour of IN740H alloy was studied by conducting experiments in a thermogravimetric analyser in the presence of air and synthetic flue gas in the temperature range of 760–900 °C. SEM/XRD/EPMA/Raman spectroscopy was used for analysing surfaces/cross sections of oxidized/corroded specimens. The oxide layer consists of Ti-doped Cr₂O₃ and NiCr₂O₄ in air-oxidized specimens, whereas additional NiO and NiS form in the presence of flue gas at 900 °C. Alumina forms at the oxide/matrix interface and at 900 °C; it was followed by γ' denuded zone with dispersed (Ti, Nb)C. The kinetics of oxidation in a steady state are found to be sub-parabolic for all the conditions.

Keywords IN 740H · High-temperature oxidation · Advanced ultra-supercritical

1 Introduction

Nickel-based superalloy IN740H is a candidate material for manufacturing superheater and reheater tubes for advanced ultra-supercritical (A-USC) steam boilers in coal-fired power plants [1–6]. IN740H is considered to be a prospective alloy for manufacturing tubes for A-USC steam boilers in coal-fired power plants. Superheater and reheater tube material should have adequate oxidation resistance (= 2 mm cross-section loss in 2×10^5 h) in addition to superior mechanical

properties to withstand the stringent operating conditions in A-USC boilers [6]. The improvement in efficiency over ~ 50% can be brought by operating the boilers at the steam temperature of 760 °C and pressures of 35 MPa [1]. During operations, the metal surface temperature of superheater and reheater tubes may reach 800 °C or even more [7, 8]. The damage mode in the superheater/reheater tubes is reported to be a combination of creep, oxidation, and hot corrosion [7–11]. However, the possibility of running the plants with frequently reduced load introduces thermal transient leading to thermal fatigue [1, 2, 12]. Therefore, the deformation and damage result from the combined effect of creep and fatigue. The final damage is ascribed to the combined action of creep, fatigue, oxidation, and hot corrosion. It is known that the surface condition has a major role, as thermal fatigue cracks mostly initiate at the surface [12–14]. For example, Sahu et al. [12], in their study on fatigue and hot corrosion interaction in alloy Nimonic 263 have shown that fatigue cracks were initiated at the sites where the protective chromium oxide layer was destroyed by the hot corrosive media. Moreover, creep voids and cavitations ultimately result from the grain boundary attack and deterioration at the surface as shown by Bagui et al. [14]. It is also known that the composition has a considerable effect on the oxidation and hot corrosion behaviour of these alloys. For example, it has been reported by Cruchley et al. [15] that the oxidation kinetics of the outer chromia layer in the temperature range of 600–900 °C was faster for Ti-doped chromia in comparison with Ti-free chromia in nickel-based superalloy RR1000. Wang et al. [16] have shown that the Cr diffusion was enhanced in the presence of Ni in Co-17Re-23Cr alloy at high temperature and the protective chromia layer growth was promoted.

With such complex interacting damage modes [13, 14] and with the fact that altering the alloy composition has a

✉ R. K. Singh
randhir.meta@mniit.ac.in

¹ Malaviya National Institute of Technology Jaipur,
Rajasthan 302 017, India

² CSIR-National Metallurgical Laboratory,
Jamshedpur 831007, India

significant effect on high-temperature oxidation resistance [15, 16], it is essential to ascertain the type of oxide scale formed in the newly developed nickel-based superalloy IN740H. Moreover, research on the oxidation behaviour of IN740H is very scarce, though few researchers reported the high-temperature oxidation and hot corrosion behaviour of Inconel 740 [7–11]. Zhao et al. [7] have carried out the oxidation of Inconel 740 in air between 850 and 1000 °C to investigate the oxidation behaviour. The formation of Cr₂O₃, TiO₂, Al₂O₃, and (Ni, Co) Cr₂O₄ has been reported [7–11]. Aung et al. [10] have studied the effect of SO₂ in flue gas at 750 °C by high-temperature electrochemical sensor and found that sulphidation attack was more pronounced in the flue gas atmosphere with SO₂. The present study highlights the isothermal oxidation behaviour of alloy IN740H in air and synthetic flue gas atmosphere at 760 °C, 800 °C, and 900 °C. Isothermal oxidation studies have been carried out in a thermogravimetric analyser (TGA) to study the oxidation kinetics and oxide formation when exposed to the above-mentioned temperature range in air and synthetic flue gas atmosphere. The surface oxides have been extensively characterized by scanning electron microscopy (SEM), X-ray diffraction (XRD) analysis, and Raman spectroscopy. The cross section of the oxide layer was analysed by electron probe microanalysis (EPMA), and line scans were done to generate the profile of elements distribution present across the oxide layer.

2 Experimental Procedure

The material was received in the form plate of 25.4 mm thickness in hot-rolled, solution-annealed, and age-hardened condition. The as-received plates were solutionized at 1120 °C for 1 h aged at 800 °C for 4 h and then air-cooled to generate the typical microstructure in which it is put into service. As per the Manufacturer's data [6], the recommended temperature range for hot-forming operations such as forging or hot-rolling is between 870 and 1190 °C. Annealing practices are described in ASME code case 2702, which specifies a temperature of 1100 °C minimum, for 1 h per one inch (25.4 mm) of thickness but not less than 30 min. The annealing range may extend as high as 1160 °C. Specific annealing conditions will be dependent upon the product form and intended application. Ageing shall be performed at a temperature between 760 °C and 815 °C, for a minimum of 4 h. The minimum ageing time shall be increased for thicknesses above 2 inches (50.8 mm) at a rate of ½ hour

per inch of additional thickness. Ageing shall be followed by air cooling. The alloy has a two-phase microstructure consisting of γ (nominally Ni, Co) matrix and approximately an 18% volume fraction of γ' precipitates (nominally Ni₃[Al, Ti]). The chemical composition of the as-received material is shown in Table 1.

Specimens of size 10×10×4 mm were cut by electrical discharge machining (EDM) for oxidation and hot corrosion studies from the as-received plate material. Wire-cut EDM setup (Make: Steer Engineering Pvt. Ltd.; Model: DK7712) was used for sample cutting, having axis travel (X-120 mm, Y-160 mm, Z-100 mm), and power supply (2 KW). The specimens were ground to 1200 grit size emery papers followed by polishing with alumina powder of 1 μ m. After polishing, specimens were ultrasonically cleaned in ethanol. A digital weighing balance (Metler, PGS07) was used to record the weight of the specimens before and after high-temperature oxidation experiments. The specimen was then placed in the ceramic bucket inside the TGA furnace to study the isothermal oxidation kinetics of the alloy. The high-temperature oxidation was performed in the temperature range of 760–900 °C for 100 h in the presence of laboratory-grade air and synthetic flue gas in TherMax 700 TGA (sensitivity of balance of $\pm 1 \mu$ g and temperature stability of $\pm 1 \text{ }^\circ\text{C}$). The synthetic flue gas consisted of 15%CO₂ + 3.5%O₂ + 0.25%SO₂ and balance N₂. During oxidation experiments, the flow rate of the pre-mixed flue gas and air was maintained at 80 ml min⁻¹.

The post-oxidation characterization of the oxide surface as well as a cross section of the oxide scales was done using FEI Nova nano SEM-430 equipped with an energy-dispersive X-ray microanalysis (EDX). For cross-sectional analysis of the oxide layer, one side of the specimens was ground to 1200 grit size emery papers followed by polishing with 0.5 μ m alumina powder. The cross section was examined by high-resolution SEM and EPMA (JXA-8230, JEOL) to measure the oxide thickness and study the cross-section morphology of the oxide layer. A line scan was performed across the oxide layer by EPMA to know the elemental distribution across the thickness of the oxide layer. Prior to SEM and EPMA analysis, X-ray diffraction (XRD) analysis and Raman spectroscopy of the surface oxides were performed. XRD was done on a D8 Discover, Bruker XRD system using Cu K α radiation, indexed between 2 θ values 20–100°. Raman spectroscopy was also done to confirm the oxides formed on the surface of oxidized specimens. The Raman spectroscopic studies were done using Alpha 300R Confocal Raman Microscope, WiTech GmbH, having a wavelength of 532 nm, and a charged coupled device

Table 1 Chemical composition of as-received material

Element	Ni	Cr	Co	Al	Ti	Nb	Mo	Mn	Fe	Si	C
wt%	50.14	24.57	20.09	1.33	1.33	1.46	0.35	0.25	0.15	0.17	0.02

(CCD) detector with grating size (600 g/mm), and spectral resolution down to 0.1 cm⁻¹. All the spectra recorded each spot on the surface of the samples for 10 s.

3 Results and Discussion

3.1 Gravimetric Oxidation Kinetics

The change in the specific weight of specimens oxidized in air and flue gas in the temperature range of 760 and 800 °C for 100 h is shown in Fig. 1a, b. It is observed that there is a rapid mass gain in the initial 2–3 h of the transient stage of oxidation in all the oxidizing conditions. The graphs also reveal the higher oxidation rate during the transient period of oxidation. The thickness of the oxide layer or the depth of oxidation depends on temperature and the duration of the initial transient state of oxidation. After the transient period, a uniform layer of oxides is formed and thus the oxidation rate slows down. During steady-state conditions, the rate of oxidation is slow. Figure 2 shows the change in the specific weight of specimens oxidized in air and flue gas at 900 °C. At 900 °C, the initial gain in mass is almost five times higher than the mass gain at 760 and 800 °C and it also shows two slopes in the stable region during oxidation in flue gas. The mass gain in the case of synthetic flue gas specimens is higher in comparison with specimens oxidized in the air at all the tested temperatures. The oxidation kinetics can be described by examining the growth-time constant, *n* which is the exponent in Eq. (1)

$$\left(\frac{\Delta w}{A}\right) = k_p t^n + C \tag{1}$$

where ($\Delta w/A$) is the oxidation mass per unit surface area, *t* is oxidation time in s, and *C* is constant.

The value of *n* is obtained from the slope of the log–log plot and is indicative of the mechanism controlling the

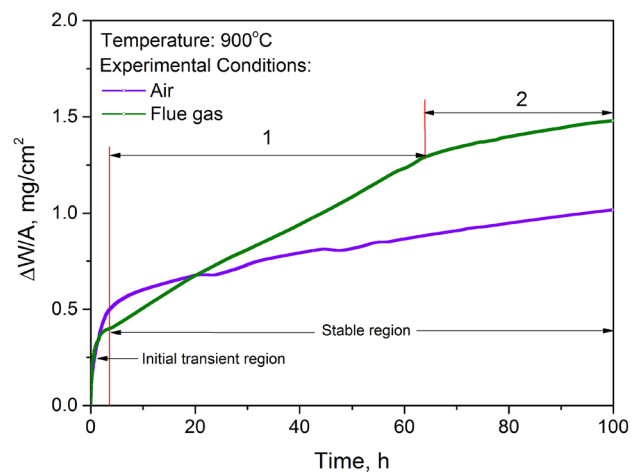


Fig. 2 Weight change per unit area of the specimen oxidized in air and flue gas atmosphere at 900 °C

oxidation rate. The exponent *n* values obtained for all oxidizing conditions at each temperature are collated in Table 2. If the value of *n* < 0.5, it is sub-parabolic, and if *n* = 0.5 then it is parabolic growth kinetics. It is said to be linear if the value of *n* = 1. The exponent *n* value was also verified by nonlinear curve fitting of the oxidation weight gain curves. It was found to follow the power function $y = ax^b$ ($a > 0, 0 < b < 1$). The exponent *b* values are depicted in Table 2. The parameter *b* decides the ability of curves to be stable with time. The power function becomes parabolic if exponent *b* is 0.5 [17]. The exponent *n* values of the steady state and *b* values obtained are the same as evident from Table 2. In the present investigation, both exponent values are less than 0.5, and thus, the oxidation kinetics is sub-parabolic in all the oxidizing conditions at all the investigated temperature ranges in the steady-state condition except the specimen oxidized

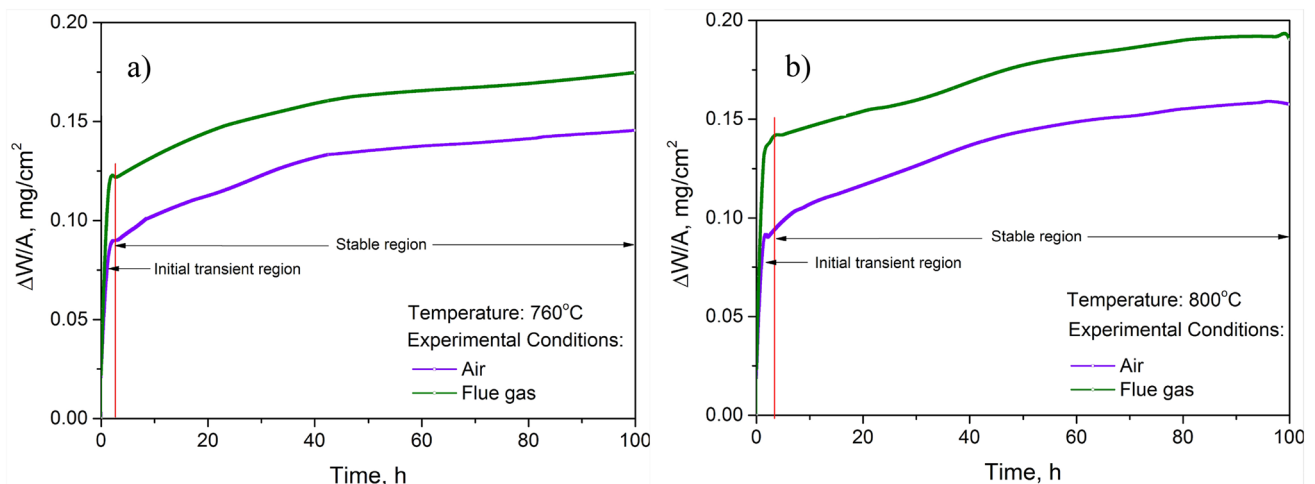


Fig. 1 Weight change per unit area of the specimens oxidized in air and flue gas atmosphere at **a** 760 °C and **b** 800 °C

Table 2 The parabolic rate constant and the exponent values in steady-state region

Oxidation conditions	Temperature (°C), time (h)	k_p (mg cm ⁻² s ⁻⁴)	Exponent n value	Exponent b value
Oxidized in air	760 °C, 100 h	3.30×10^{-8}	0.15	0.15
	800 °C, 100 h	4.58×10^{-8}	0.18	0.18
	900 °C, 100 h	2.09×10^{-6}	0.22	0.24
Oxidized in synthetic flue gas	760 °C, 100 h	3.74×10^{-8}	0.11	0.12
	800 °C, 100 h	5.43×10^{-8}	0.12	0.13
	900 °C, 100 h	6.74×10^{-6} (1) 3.98×10^{-6} (2)	0.48	0.49

in the flue gas atmosphere at 900 °C, which has the n value closer to 0.5 and seems to follow parabolic kinetics.

The oxidation kinetics of Ni–Cr–Al-based superalloys usually follow the parabolic rate law as given in Eq. (1) [11–13]. The parabolic rate constant is calculated using Eq. (2).

$$\left(\frac{\Delta w}{A}\right)^2 = k_p t \quad (2)$$

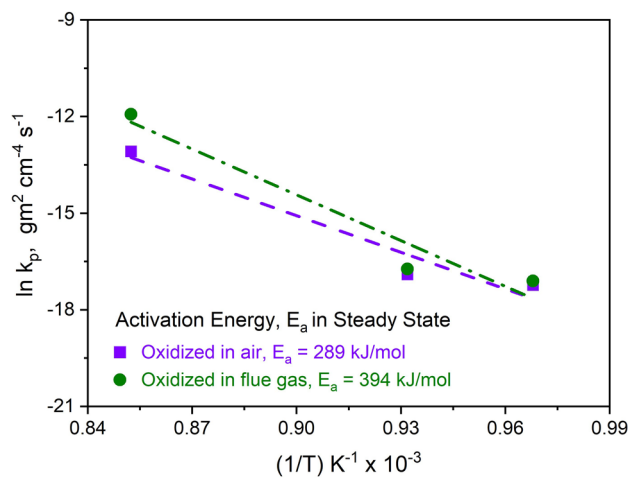
where k_p represents the parabolic rate constant and $(\Delta w/A)$ is the specific weight gain of the specimens for exposure time, t . The calculated k_p values are listed in Table 2 for all the oxidizing conditions. Parabolic oxidation kinetics signify that a thermal diffusion process is rate determining. Such a process may include a uniform diffusion of one or more than one reactant through the growing compact scale. The parabolic rate constant which can be represented as a temperature dependent function by using an Arrhenius equation is shown in Eq. (3).

$$k = Ae^{-E_a/RT} \quad (3)$$

where k is the rate constant, E_a is activation energy (kJ mole⁻¹), T is the temperature (K), R is ideal gas constant (8.3145 J/K⁻¹ mol⁻¹), and A is the frequency or pre-exponential factor.

Both A and E_a are specific to a given reaction. The plot of k_p versus the inverse of temperature results in a straight line the slope of which gives the activation energy of the reaction. The linear expression is obtained by taking the log on both sides. The term activation energy is not rigorously correct as it involves more than one element. However, it is useful as it describes the temperature dependence reaction kinetics.

The slope of the plot of $\ln k$ versus the inverse of temperature ($1/T$) gives the activation energy values as shown in Fig. 3. It is observed that the reaction with higher activation energy, E_a , has a steeper slope. So, the reaction rate is very sensitive to temperature change. In contrast, in the reaction with lower activation energy, E_a is less sensitive to

**Fig. 3** Arrhenius plots corresponding to oxidation of alloy IN740H in air and flue gas atmosphere at temperatures 760, 800, and 900 °C**Table 3** Activation energy, E_a in steady-state region

Oxidation conditions	E_a (kJ/mol)
Oxidized in air	289
Oxidized in synthetic flue gas	394

temperature change. The obtained activation energy values under different oxidizing conditions are given in Table 3. It is observed that the activation energy values for specimens oxidized in flue gas are 394 kJ mol⁻¹ and in air 289 kJ mol⁻¹, respectively. The value of the specimen oxidized in flue gas is higher than in the air atmosphere, indicating that the oxidation in flue gas is more sensitive to the temperature.

3.2 Characterization of Oxides

3.2.1 Air Atmosphere

Figure 4a shows the XRD patterns of the oxide scale formed on the specimens subjected to isothermal exposure in the

temperature range of 760–900 °C in air. From the XRD analysis, it is evident that the Ti-doped Cr₂O₃ and NiCr₂O₄ spinel are present in the oxide scales formed during isothermal oxidation. The specimen surface oxidized in the air atmosphere at all the investigated temperatures was also identified and analysed by Raman spectroscopy. The oxides found by Raman spectroscopy are listed in Table 4. A representative Raman analysis confirming the presence of Cr₂O₃, NiCr₂O₄, and TiO₂ on a specimen oxidized in air is shown in Fig. 5a.

It is observed that surface oxide morphology changes with oxidizing temperature. SEM images revealing the surface oxide morphology of IN740H specimens oxidized in air at the temperature of 760–900 °C are shown in Fig. 6. The EDS analysis of the oxide scale of specimens oxidized in air shows Cr-, Ti-, and Ni-rich oxides on the surface.

Figure 7 shows the EPMA mapping of a cross section of the specimen oxidized in air at 760 °C which reveals that Ti-doped chromia formation on the outer oxide layer followed by alumina at the interface of matrix and oxide layer. A very

thin layer of ~ 1 μm of mixed oxides of Ti-doped Cr₂O₃ is formed on the specimen. At 800 °C, ~ 5-μm-thick oxide layers consisting of Ti-doped Cr₂O₃ and NiCr₂O₄ sandwiched between the outer oxide layer and the matrix is observed. Figure 9a shows the cross section of the specimen oxidized in air at 900 °C. The thickness of the oxide scale is ~ 10 μm consisting of Ti-doped Cr₂O₃ formed on the outer layer and NiCr₂O₄ as the intermediate layer, followed by Al₂O₃ at the interface of oxide/matrix. (Ti, Nb)C and oxide protuberance is observed in the adjacent matrix region of γ' denuded zone.

The average oxide thickness is collated in Table 5. Due to the high Cr fraction in the alloy, Cr₂O₃ was formed during the initial stage of oxidation. From the EPMA line analysis shown in Fig. 10a, it is observed that complex oxides are formed on specimens at different temperatures. The diffusivity of elements like Ti and Al increases with an increase in temperature. The formation of oxides depends on the alloying elements (such as Cr and Al) and the diffusion process. Due to the high affinity of aluminium towards oxygen,

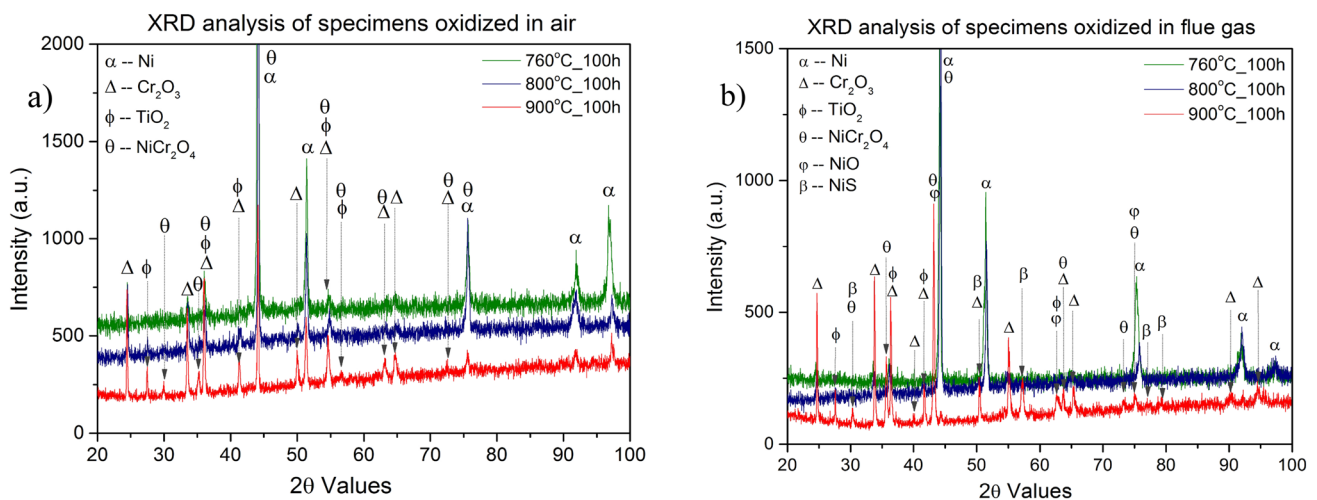


Fig. 4 XRD plots showing different oxides formed during oxidation of alloy IN740H at 760, 800, and 900 °C: **a** in air and **b** flue gas atmosphere

Table 4 Oxides confirmed by Raman analysis

Species [Ref]	Specimen oxidized in air			Specimen oxidized in flue gas		
	760 °C	800 °C	900 °C	760 °C	800 °C	900 °C
Cr ₂ O ₃ [18–21]	352, 393, 555	305, 346, 398, 528, 554	305	528, 613	524	311
NiCr ₂ O ₄ [20, 22, 23]	189, 193, 430, 514, 559, 617, 795,	559	689	510, 613, 690	–	–
NiO [20, 24]	367, 509, 555, 725, 919,	728, 554, 908	919, 1069	510	725	–
TiO ₂ [25–27]	193, 509	143, 198, 398, 642, 443, 449	197, 403, 449	451, 511, 613	198	195, 239, 444
NiFe ₂ O ₄ [23, 28]	189, 484, 650, 657, 662, 698, 706	695, 706	188, 460, 492	451	457, 566, 666, 701	566, 655, 703

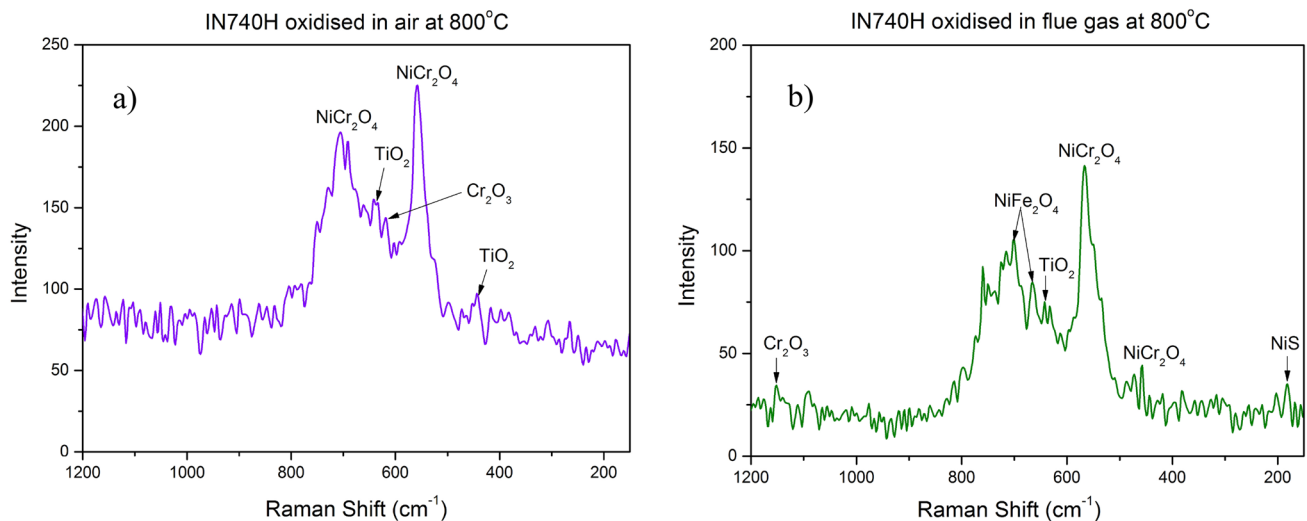


Fig. 5 Raman peaks found on specimen oxidized at 800 °C: **a** in air and **b** in flue gas atmosphere

aluminium from the γ' diffuses out and thus forms Al₂O₃ at the interface [17].

3.2.2 Flue Gas Atmosphere

The XRD analysis of specimens exposed to the flue gas atmosphere in the temperature range of 760–900 °C shows the presence of Ti-doped Cr₂O₃, NiCr₂O₄, and NiO phases along with nickel sulphide (NiS) phase as shown in Fig. 4b. The existence of NiO and NiS phases is observed only on the specimen oxidized at 900 °C. The Raman analysis also confirms the presence of NiS on specimens oxidized in flue gas and is shown in Fig. 5b.

The surface morphology observed under SEM of the specimen oxidized at 760–900 °C is shown in Fig. 8. The oxide morphology of the specimen oxidized in flue gas shows a dense chromia oxide when compared to the specimen oxidized in air. Sulphur was also traced in the EDS analysis on the surface layer of the specimen. In the flue gas atmosphere at 760 °C, ~1- μ m thin layer of Ti-doped chromia is observed on the specimen. The Cr₂O₃ layer thickness increases with an increase in temperature. At 800 °C, also a thin layer of ~1.5 μ m thickness of similar oxides was observed on the specimen. The oxide layer thickness at 900 °C is ~15 μ m, and oxide thickness at all the temperatures is compiled in Table 5. It clearly indicates that the thickness of the oxide layer formed at 760 and 800 °C is less, while there is a drastic change in oxide thickness at 900 °C. Figure 9b and 10b shows the cross-section oxide morphology and line scans of the specimen oxidized in flue gas at 900 °C, respectively. At 900 °C (Ni, Co), Cr₂O₄ spinel is formed as an outer layer and Al₂O₃ at the oxide/matrix interface followed by γ' denuded zone.

3.3 Discussion

The formation of oxides depends on the alloying elements (such as Cr and Al) and the diffusion process. Oxidation generally starts with the nucleation of NiO and Cr₂O₃ and by the end of the transient state a continuous layer of Cr₂O₃ forms [29]. Cr₂O₃ is stoichiometric oxide, so diffusion is low. Cr₂O₃ is a protective layer. The anti-exfoliating ability of scale is improved by the presence of Cr₂O₃, and the oxidation resistance of an alloy is strengthened by the presence of Al₂O₃ and SiO₂ [17]. Ti-rich oxides are known to form on the outer surface of the chromia layer. The ability of chromia to dissolve titanium in the oxidized state has been known for some time. It is likely that titanium is incorporated as the Ti⁴⁺ ion since this has minimal effect on the chromia lattice spacing [15]. The diffusivity of elements like Ti and Al increases with an increase in temperature. Due to the high affinity of aluminium towards oxygen, aluminium from the γ' gets dissolved in the matrix and diffuses towards the outer layer. The Al³⁺ reacts with O²⁻ forms Al₂O₃ at the interface [17], thus forming γ' denuded zone. Al oxidizes extensively internally, permitting Cr to diffuse to the alloy–oxide interface and maintain the Cr₂O₃ layer; rather, it oxidizes internally. The Cr₂O₃ supplies O₂ for the formation of Al₂O₃ internally. However, the dissociation pressure of Cr₂O₃ is low and is sufficient to cause the formation of Al₂O₃ beneath the Cr₂O₃ layer, leading to a substantially slow oxidation rate in the later stage [30].

In the presence of flue gas, high SO₃ partial pressure is required to stabilize the low-melting-point solution of sulphates to sustain the hot corrosion during the propagation stage [8]. The depletion of Cr and Al oxide takes place due to higher ion activity as it forms basic flux and thereby

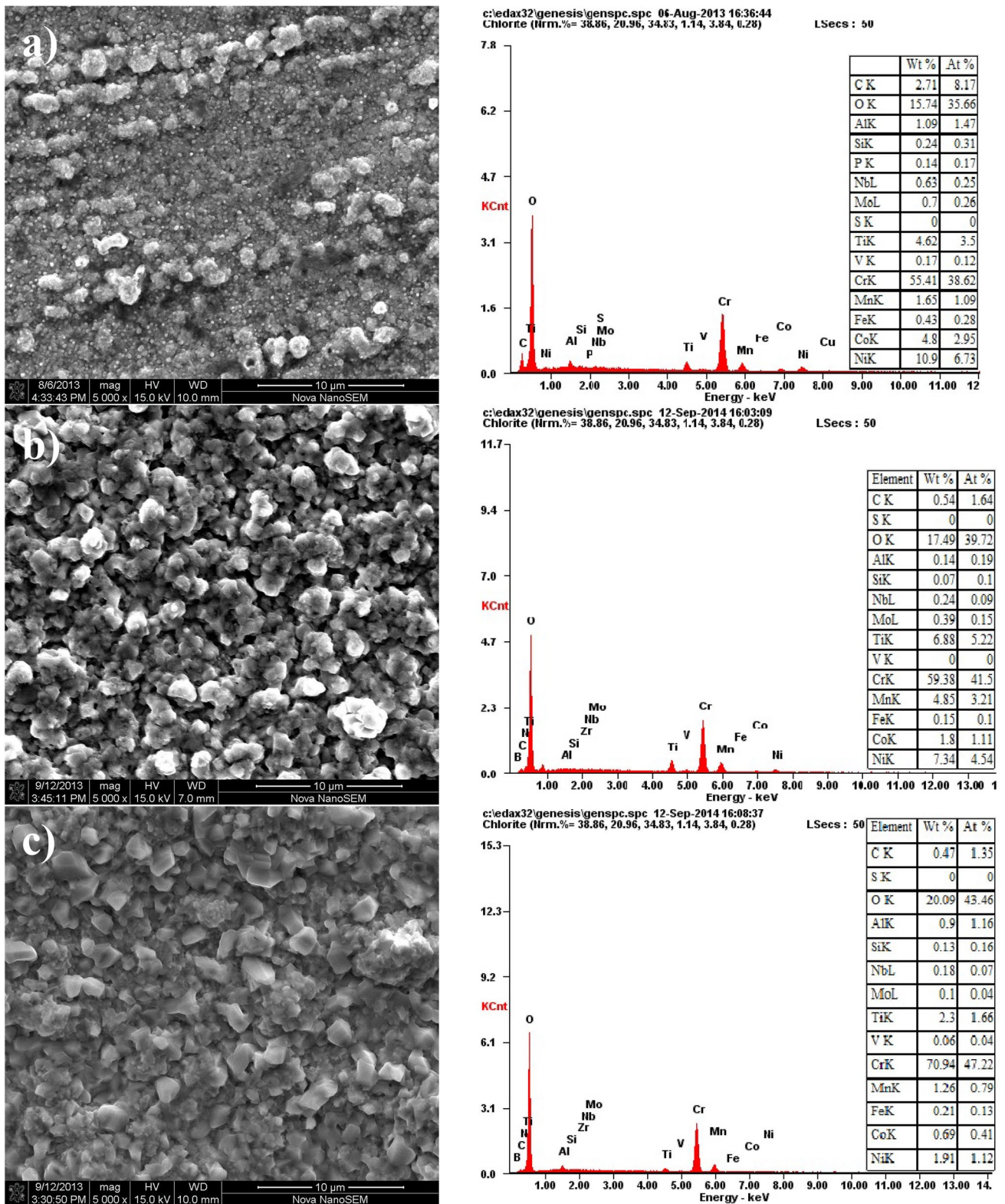


Fig. 6 SEM images showing the surface oxide morphology on the specimens oxidized in laboratory air at **a** 760 °C; **b** 800 °C; **c** 900 °C and the corresponding bulk EDS plots

Fig. 7 EPMA EDS elemental mapping of specimen oxidized in air at 760 °C

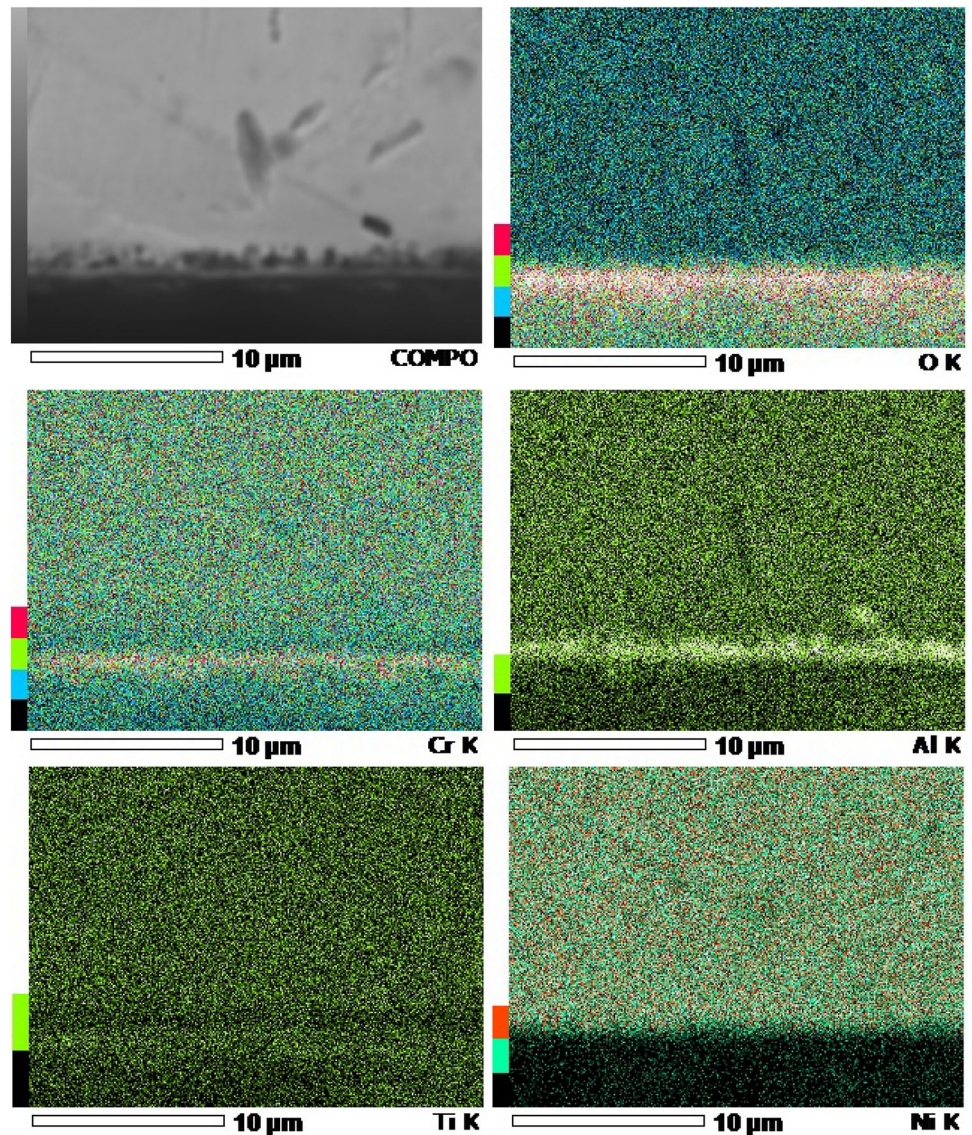


Table 5 Average thickness, µm of oxide layer

Oxidation conditions	Temperature (°C—Time, h)	Avg. oxide layer thickness (µm)
Specimen oxidized in the air	760 °C–100 h	1.0
	800 °C–100 h	3.0
	900 °C–100 h	10.7
Specimen oxidized in synthetic flue gas	760 °C–100 h	1.3
	800 °C–100 h	1.6
	900 °C–100 h	15.7

increases the oxidation rate than in normal oxidation. During the steady state, the oxidation rate slows down as thick Cr_2O_3 formed on the surface prevents fluxing with sulphates, and as a result, there is a meagre presence of sulphur in the

oxide layer. Thus, the depletion of Cr_2O_3 also slows down and reduces the inward diffusion of sulphur in the forms of S, S^{2-} , SO_2 , etc. The specimens up to 800 °C show slow oxidation kinetics, whereas at 900 °C the sulphur accelerates the oxidation rate. The influence of different elements on the high-temperature oxidation process will depend on the particular mechanism of accelerated oxidation that is operative.

4 Conclusions

- (i) The oxidation rate was higher in the specimens oxidized in the flue gas atmosphere due to the diffusion of sulphur.
- (ii) From the obtained n values, it is found that the rate of oxidation is almost sub-parabolic in the steady state.

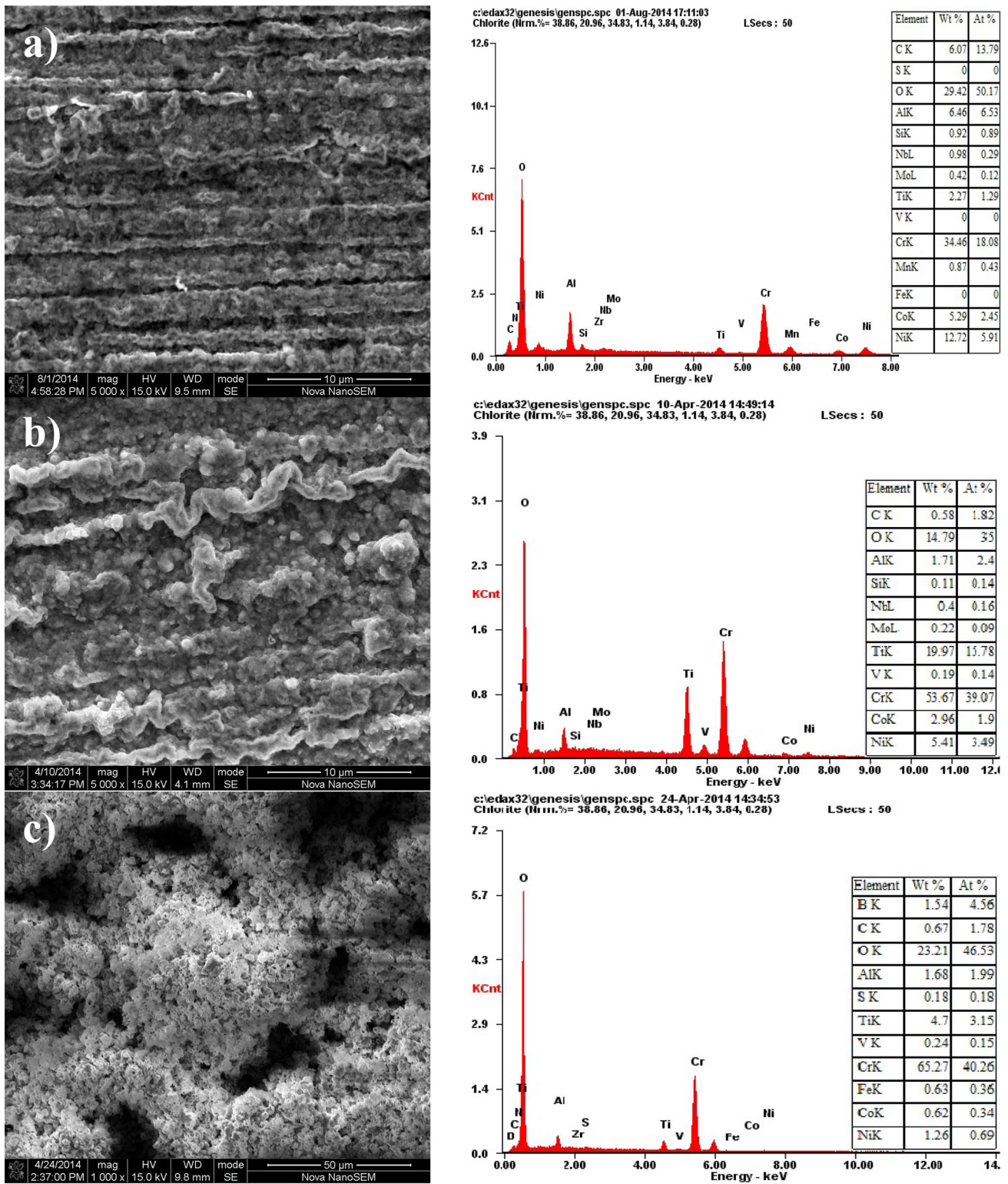


Fig. 8 SEM images showing the surface oxide morphology on the specimens oxidized in flue gas at **a** 760 °C; **b** 800 °C; **c** 900 °C and the corresponding bulk EDS plots

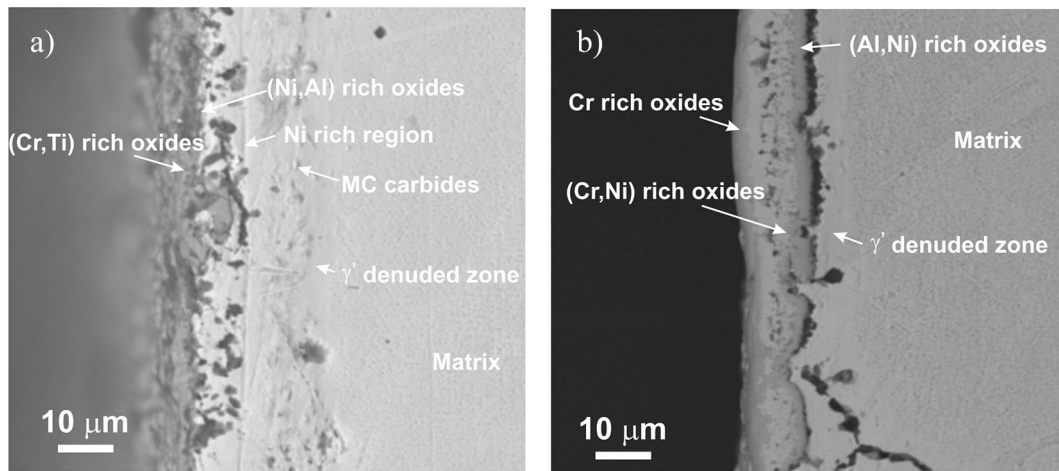


Fig. 9 EPMA images of cross section of specimens oxidized under air and flue gas at 900 °C indicating the possible phases formed: **a** specimen oxidized in the air; **b** specimen oxidized in flue gas

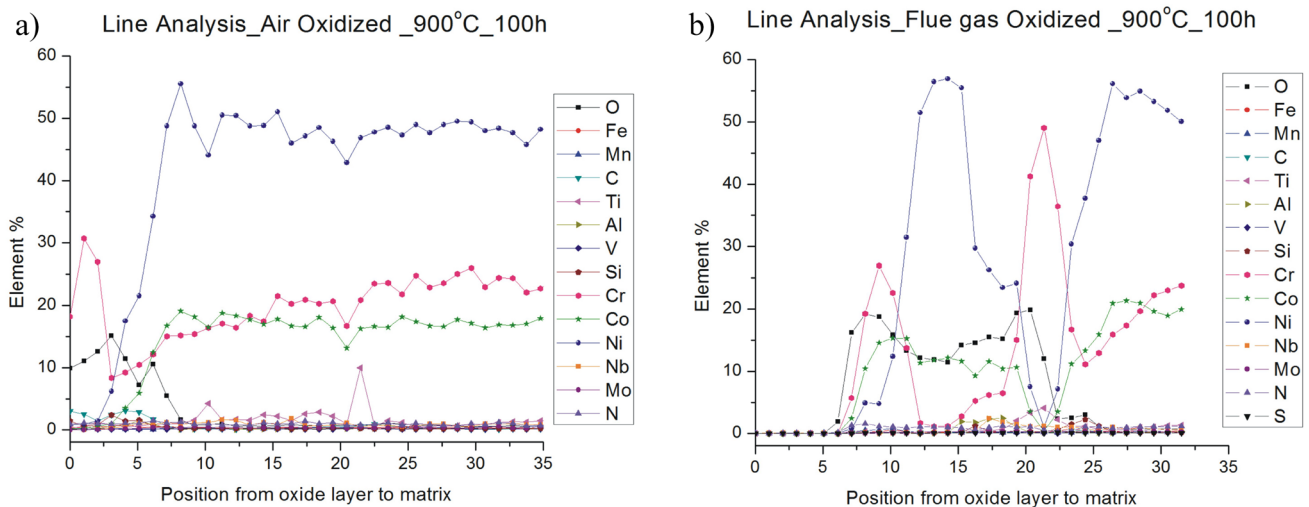


Fig. 10 EPMA line analysis of a cross section of specimens oxidized under air and flue gas at 900 °C **a** specimen oxidized in air **b** specimen oxidized in flue gas

- (iii) The thickness of the oxide layer formed mainly depends on the temperature and the duration and rate of oxidation in the transient period.
- (iv) The oxide thickness formed at 900 °C was five times that of the thickness of oxide formed at 760 °C and 800 °C.
- (v) Oxide protuberance and MC type carbides in γ' denuded zone were prominent at 900 °C in specimen oxidized in air, while in flue gas, only γ' denuded zone formation was observed.

study and CSIR-National Metallurgical Laboratory, Jamshedpur, India, for providing the facilities to carry out the experiments and characterization.

Declarations

Conflict of interest The authors whose names are listed immediately below title of manuscript certify that they have NO affiliations with or involvement in any organization or entity with any financial interest or non-financial interest in the subject matter or materials discussed in this manuscript.

Acknowledgements The authors thank Special Metals Corporation, Huntington WV, USA, for providing the materials used in this

References

1. Viswanathan R, Henry J F, Tanzosh J, Stanko G, Shingledecker J, Vitalis B, and Purgert R, *J Mater Eng Perform* **14** (2005) 281. <https://doi.org/10.1361/10599490524039>
2. Viswanathan R, Coleman K, and Rao U, *Int J Pressure Vessels Pip* **83** (2006) 778. <https://doi.org/10.1016/j.ijpvp.2006.08.006>
3. Baker B A, Smith G D, Corrosion Resistance of Alloy 740 as Superheater Tubing in Coal-Fired Ultra-Supercritical Boilers, Paper presented at the CORROSION 2004, New Orleans, Louisiana (2004)
4. Xie X S, Zhao S Q, Dong J X, Smith G D, Baker B A, and Patel S L, *Adv. Mater. Technol. Fossil Power Plants* (2008). <https://doi.org/10.1361/cp2007epri0220>
5. Yan C, Zheng L, Godfrey A, Wei L, and Yuqing W, *Mater Sci Eng A* **589** (2014) 153. <https://doi.org/10.1016/j.msea.2013.09.076>
6. Inconel Alloy 740H, A Superalloy Specifically Designed For Advanced Ultra Supercritical Power Generation, <https://www.specialmetals.com/documents/technical-bulletins/inconel-alloy-740h.pdf>, Accessed December 2022.
7. Zhao S, Xie X, and Smith G D, *Surface Coat Technol* **185** (2004) 178. <https://doi.org/10.1016/j.surfcoat.2003.12.003>
8. Zhao S, Xie X, Smith G D, and Patel S J, *Mater Chem Phys* **90** (2005) 275. <https://doi.org/10.1016/j.matchemphys.2004.04.006>
9. Stein-Brzozowska G, Flórez D M, Maier J, and Scheffknecht G, *Fuel* **108** (2013) 521. <https://doi.org/10.1016/j.fuel.2012.11.081>
10. Aung N N, *Corrosion Sci.* **76** (2013) 390. <https://doi.org/10.1016/j.corsci.2013.07.012>
11. Aung N N, *Corrosion Sci* **82** (2014) 227. <https://doi.org/10.1016/j.corsci.2014.01.020>
12. Sahu J K, Ravi Kumar B, Das S K, Paulose N, and Mannan S L, *Mater Sci Eng A* **622** (2015) 131. <https://doi.org/10.1016/j.msea.2014.11.016>
13. Sahu J K, Gupta R, Swaminathan J, Paulose N, and Mannan S L, *Int J Fatigue* **51** (2013) 68. <https://doi.org/10.1016/j.ijfatigue.2013.02.006>
14. Bagui S, Ray A K, Sahu J K, Parida N, Swaminathan J, Tamilselvi M, and Mannan S L, *Mater Sci Eng A* **566** (2013) 54. <https://doi.org/10.1016/j.ijfatigue.2013.02.006>
15. Cruchley S, Evans H E, Taylor M P, Hardy M C, and Stekovic S, *Corros Sci* **75** (2013) 58. <https://doi.org/10.1016/j.corsci.2013.05.016>
16. Wang L, Gorr B, Christ H-J, Mukherji D, and Rösle J, *Corros Sci* **93** (2015) 19. <https://doi.org/10.1016/j.corsci.2015.01.004>
17. Wang H, Yu H, Wang Z, Zhang J, Chen H, Min G, *J Wuhan Univ Technol Mat Sci Edit* **25** (2010) 99. <https://doi.org/10.1007/s11595-010-1099-3>
18. Thierry D, Persson D, Leygraf C, Delichere D, Joiret S, Pallotta C, and Hugot-leGof A, *J. Electrochem. Soc.* **135** (1988) 305. <https://doi.org/10.1149/1.2095605>
19. Beattie I R, and Gilson T R, *J. Chem Soc. A* (1970). <https://doi.org/10.1039/J19700000980>
20. Kim JH, Hwang IS, In-situ Raman spectroscopic study of oxide films on alloy 600 in simulated PWR water, *Proceedings of the Korean Nuclear Spring Meeting Gyeongju, Korea* (2003)
21. McCarty K F, and Boehme D R, A Raman study of the systems Fe₃-, Crx₀₄ and Fez- & rx₀₃. *J. Solid State Chem* **79** (1989) 19. [https://doi.org/10.1016/0022-4596\(89\)90245-4](https://doi.org/10.1016/0022-4596(89)90245-4)
22. Wang Z, Saxena S K, Lazor P, and O'Neill H S C, *J Phys Chem Solids* **64** (2003) 425.
23. Hosterman BD, Raman spectroscopic study of solid solution spinel oxides, UNLV theses/ dissertations/professional papers/ Capstones (2011) 1087. https://digitalscholarship.unlv.edu/these_dissertations/1087/ accessed 18 Sept 9 2023
24. Srnanek R, Hotovy I, Malcher V, Vincze A, McPhail D, Littlewood S, A Raman study of NiO/sub x/ films for gas sensors applications, ASDAM 2000. Conference Proceedings. Third International Euro Conference on Advanced Semiconductor Devices and Microsystems (Cat. No. 00EX386), Smolenice, Slovakia, (2000) p 303. <https://doi.org/10.1109/ASDAM.2000.889506>
25. Šćepanović M J, Grujić-Brojčin M, Dohčević-Mitrović Z D, and Popovic Z V, *Sci Sinter* **41** (2009) 67. <https://doi.org/10.2298/SOS0901067S>
26. Aprile C, Maretti L, Alvaro M, Scaiano J C, and Garcia H, *Dalton Trans.* **28** (2008) 5389. <https://doi.org/10.1039/B807453D>
27. Hemley R J, Mao H-K, and Bell P M, *Physica B C* **139** (1986) 455. [https://doi.org/10.1016/0378-4363\(86\)90621-2](https://doi.org/10.1016/0378-4363(86)90621-2)
28. Kim Ji Hyun, and Soon Hwang I I, *Nuclear Eng Design* **235** (2005) 1029. <https://doi.org/10.1016/j.nucengdes.2004.12.002>
29. Berthod P, *Oxid Met* **64** (2005) 235. <https://doi.org/10.1007/s11085-005-6562-8>
30. Stott F H, and Wood G C, *Corros Sci* **11** (1971) 799. [https://doi.org/10.1016/S0010-938X\(71\)80044-6](https://doi.org/10.1016/S0010-938X(71)80044-6)

Publisher's Note Springer Nature remains neutral with regard to jurisdictional claims in published maps and institutional affiliations.

Springer Nature or its licensor (e.g. a society or other partner) holds exclusive rights to this article under a publishing agreement with the author(s) or other rightsholder(s); author self-archiving of the accepted manuscript version of this article is solely governed by the terms of such publishing agreement and applicable law.